Research Square

Preprints are preliminary reports that have not undergone peer review.
They should not be considered conclusive, used to inform clinical practice,
or referenced by the media as validated information.

In Situ Synthesis of Mn-Doped CoP@Ni2P Nanoneedles as a High-Performance Bifunctional Electrocatalyst for Efficient Water Splitting

Yu Dong
Shenyang Ligong University
Xuan Zhao
Shenyang Ligong University
Zhijie Wang
Shenyang Ligong University
Ende Wang
Shenyang Ligong University
Yusheng Qiu
Shenyang Ligong University
Naikun Sun
Shenyang Ligong University
Yongli Tong
tyl.tongyongli@163.com

Shenyang Ligong University

Research Article

Keywords: Mn-doped CoP@Ni2P, HER, OER, overall water splitting, bifunctional electrocatalyst

Posted Date: April 7th, 2026

DOI: https://doi.org/10.21203/rs.3.rs-9176655/v1

License: This work is licensed under a Creative Commons Attribution 4.0 International License.
Read Full License

Additional Declarations: No competing interests reported.

Abstract

The development of efficient and low-cost bifunctional electrocatalysts for overall water splitting is crucial for sustainable hydrogen production. In this work, we report the in situ synthesis of Mn-doped CoP@Ni_2P nanoneedle arrays supported on nickel foam as a high-performance electrocatalysts for both the hydrogen evolution reaction (HER) and the oxygen evolution reaction (OER). The catalyst is composed of vertically aligned nanoneedles, which provide abundant active sites and facilitate charge transfer. Benefiting from the electronic modulation induced by Mn doping and the synergistic effect of the CoP@Ni_2P heterostructure, the optimized Mn-CoP@Ni_2P electrode exhibits exceptional catalytic activity, delivering low overpotentials of 61.7 mV for the HER and 122.0 mV for the OER at 10 mA cm^{-2} in 1.0 M KOH. Impedance and relaxation-time analyses reveal faster and more homogeneous interfacial electron transfer after Mn incorporation. Furthermore, systematic measurements across acidic and alkaline electrolytes demonstrate stable catalytic responses over a wide pH range, indicating that the heterostructure effectively accommodates proton- and hydroxide-mediated reaction pathways. Moreover, when employed as both the anode and the cathode in a two-electrode electrolyzer, the assembled device only requires a cell voltage of 1.48 V to deliver a current density of 10 mA cm^{-2}. This work provides a promising strategy for the design of non-precious metal electrocatalysts with optimized performance for efficient overall water splitting.

1 Introduction

The global energy system faces increasing challenges associated with fossil fuel depletion and climate change, driving the demand for sustainable energy carriers. Hydrogen produced via water electrolysis is widely recognized as a promising clean energy carrier; however, current industrial hydrogen production still largely relies on fossil fuels. Therefore, the development of efficient and cost-effective electrolysis technologies is crucial for enabling large-scale green hydrogen production [1–3]. Electrochemical overall water splitting (OWS) involves hydrogen evolution reaction (HER) and oxygen evolution reaction (OER). Despite a theoretical cell voltage of 1.23 V, the sluggish reaction kinetics (especially for the multi-step OER process) result in high overpotentials, which significantly increases the energy consumption of electrolysis [4–7]. Noble-metal catalysts such as Pt, IrO_2, and RuO_2 exhibit excellent catalytic performance, but their high cost, scarcity, and poor stability at high current densities limit their practical application [8–10]. Consequently, significant efforts have been devoted to developing earth-abundant, non-precious bifunctional electrocatalysts that can efficiently catalyze both HER and OER in alkaline media [11, 12].

Transition metal phosphides (TMPs) have attracted considerable attention owing to their metallic conductivity, tunable electronic structures, and hydrogen adsorption properties comparable to those of noble metals [13–15]. Nickel-, cobalt-, and iron-based phosphides integrate electron-rich phosphorus with transition metals, which facilitates water dissociation and the adsorption of reaction intermediates during the HER and OER processes [16, 17]. Moreover, TMPs can undergo surface reconstruction during

OER to form catalytically active oxyhydroxide species, while the conductive phosphide framework ensures efficient charge transport. However, some obstacles like inadequate active sites and restricted charge-transfer capacity still impede their practical applications. [18].

To address these limitations, various strategies have been proposed to regulate both the structural and electronic properties of TMPs. Constructing self-supported nanoarrays—such as nanoneedles, nanosheets, and hollow structures—on conductive substrates can significantly increase the active surface area, shorten ion-diffusion pathways, and facilitate gas release [19–21]. In addition, designing heterostructures or multi-metal TMPs can modulate charge distribution and optimize adsorption energies of reaction intermediates, thereby accelerating catalytic kinetics [22]. Among these materials, CoP@Ni_2P-based heterostructures have demonstrated considerable potential as bifunctional electrocatalysts for alkaline OWS due to their high density of active sites and excellent electrical conductivity [20–22].

Another effective strategy is heteroatom doping to tune the local coordination environment and electronic structure of TMPs. In particular, Mn doping has been reported to regulate the d-band center, modify the adsorption energies of key intermediates (H*, OH*, and OOH*), and redistribute charge density along metal–P bonds, thereby lowering reaction energy barriers and improving catalytic performance [23]. Furthermore, Mn incorporation can introduce defect sites, enhance electrical conductivity, and promote the formation of catalytically active hydroxide species, leading to improved bifunctional activity.

Recently, several Mn-doped Co/Ni phosphide systems have been reported for water splitting applications. For instance, Ram et al. reported a Mn-(Co, $Ni)_2P$/CoP hybrid embedded in an N, S co-doped carbon matrix, which was prepared via hydrothermal aging followed by chemical vapor deposition. This catalyst delivered low overpotentials of 61 mV for the HER and 213 mV for the OER at 10 mA cm^{-2}, which was attributed to the synergistic interaction between Mn doping, phosphide heterointerfaces, and the conductive heteroatom-doped carbon framework [24]. Similarly, Zhang and co-workers constructed Mn-doped trimetallic (Mn)CoP_2/NiCoP ultrafine nanoparticles on carbon cloth via in-situ hydrolysis followed by low-temperature phosphidation, achieving overpotentials of 52 mV for HER and 141 mV for OER at 10 mA cm^{-2} in 1 M KOH, which was attributed to Mn-induced lattice contraction and electronic structure modulation that promoted charge transfer and catalytic kinetics [25].

In this work, Mn-doped CoP@Ni_2P nanoneedle arrays were synthesized via an in-situ strategy on nickel foam. The as-prepared catalyst exhibited a microspherical architecture assembled from radially oriented nanoneedles, which provided abundant active sites and efficient electron transport pathways. Benefiting from the synergistic effects of Mn doping and the CoP@Ni_2P heterointerface, the optimized electrode exhibits excellent HER and OER performance in 1.0 M KOH, with overpotentials of 61.7 mV and 122 mV at 10 mA·cm^{-2}, respectively. In addition, a low cell voltage of 1.48 V is achieved for overall water splitting. This study demonstrates that structural modulation combined with controlled Mn doping is an effective strategy for developing high-performance phosphide-based electrocatalysts.

2 Experimental

2.1 Chemicals and materials

All chemicals used in this work were of analytical grade purity. Cobalt nitrate hexahydrate ($Co(NO_3)_2·6H_2O$), nickel nitrate hexahydrate ($Ni(NO_3)_2·6H_2O$, 99%), urea (99%), and manganese nitrate tetrahydrate ($Mn(NO_3)_2·4H_2O$, 99%) were purchased from Macklin Biochemical Technology Co., Ltd., while ammonium fluoride (NH_4F, 99%) was purchased from Tianjin Damao Chemical Reagent Factory. Prior to the synthesis procedure, the nickel foam (NF) was subjected to a thorough cleaning process. The NF pieces were soaked in acetone and 1.0 M HCl under ultrasonic agitation, followed by successive rinsing with deionized water and absolute ethanol. A final drying step in a 60°C vacuum oven removed residual moisture and prepared the NF for subsequent growth of the catalyst layer.

2.2 Sample synthesis

Firstly 0.582 g of $Co(NO_3)_2·6H_2O$, 0.582 g of $Ni(NO_3)_2·6H_2O$, 0.52 g of $Mn(NO_3)_2·4H_2O$ (corresponding to a Co:Ni:Mn molar ratio of 2:2:2.1), 0.59 g of NH_4F, and 1.2 g of urea were dissolved in 60 mL of deionized (DI) water. Afterward, the mixed solution and the pre-treated NF were transferred into a Teflon-lined stainless autoclave (100mL) and kept at 160℃ for 8h. The obtained NiCo precursors were washed with DI water and dried at 60℃. Subsequently, $NaH_2PO_2·H_2O$ (0.5g) and the prepared precursor were annealed in a tube furnace at 350℃ for 2h under Ar atmosphere. Finally, Mn-CoP@Ni_2P catalysts were synthesized after cooling down to room temperature. For comparison, CoP was synthesized following the same procedure without adding $Ni(NO_3)_2·6H_2O$ and $Mn(NO_3)_2·4H_2O$. CoP@Ni_2P was prepared using the same conditions as Mn-CoP@Ni_2P but without the addition of $Mn(NO_3)_2·4H_2O$.

2.3 Characterization

X-ray diffraction (XRD, Bruker D8 ADVANCE, 5° min^{-1}) confirmed the crystalline features of the obtained materials. Morphological evolution and nanoscale structure details were captured through scanning electron microscopy (SEM, Regulus 8100) and transmission electron microscopy (TEM, FEI Tecnai G2 F20, 200 kV). Surface compositions and valence-state information came from X-ray photoelectron spectroscopy (XPS, Escalab 250Xi). These analyses enabled evaluation of Mn-induced electronic modulation and offered insight into the chemical environment within the CoP@Ni_2P framework.

2.4 Electrochemical measurement.

The electrochemical performance of the catalysts was evaluated using a CHI660E electrochemical workstation (Shanghai Chenhua Instruments, China). All electrochemical measurements were conducted in a conventional three-electrode configuration. The as-prepared samples served directly as the working electrodes with an effective geometric area of 1 cm^2. Linear sweep voltammetry (LSV) measurements were performed in 1.0 M KOH electrolyte at a scan rate of 0.5 mV s^{-1}. To minimize the influence of solution resistance, 90% iR compensation was applied during the measurements. Prior to recording the

polarization curves, the working electrodes were activated by continuous cycling for 300 cycles until stable LSV responses were obtained. The polarization curves were corrected for ohmic losses according to the following equation:

$E_{iR-corrected} = E - iR \times 0.9$

where $E_{iR-corrected}$ and E represent the iR-corrected and measured potentials (vs. RHE, V), respectively; i is the corresponding current (A); and R is the ohmic resistance of the electrolyte (Ω).

The Tafel slopes were calculated by fitting LSV curves:

$\eta = a + b*\log(j)$

where η represents the overpotential, j is the current density, b is the Tafel slope, and a is the intercept. The electrochemical double-layer capacitance (C_{dl}) was estimated from cyclic voltammetry (CV) measurements conducted within a non-Faradaic potential region. Electrochemical impedance spectroscopy (EIS) measurements were performed over a frequency range of 0.1 Hz to 100 kHz with an AC amplitude of 5 mV. During the EIS tests, the applied DC potentials were set at − 0.134 V (vs. RHE) for HER and 0.286 V (vs. RHE) for OER.

In tests under different pH conditions, considering NF corrodes in acidic electrolytes, Mn-CoP@Ni_2P powder was evenly coated on carbon cloth with a blend of Nafion and ethanol as the binder. Subsequently, electrochemical performance tests were performed under the same conditions in the main text.

Overall water-splitting performance was evaluated in a two-electrode alkaline cell, in which Mn-CoP@Ni_2P functioned as both anode and cathode. A Pt/C||RuO_2 pair served as a performance benchmark.

3 Results and discussion

3.1 Preparation and characterization

Figure 1 illustrates the two-step fabrication process of the Mn-CoP@Ni_2P catalyst. Initially, nanoneedles are hydrothermally deposited and aggregate onto the NF surface, forming smooth nanoneedles, which serve as the precursor for subsequent phosphorization. Subsequently, phosphating is conducted in an Ar atmosphere. During this phosphorization step, the phosphorus precursor decomposes to release reactive P_x species, which adsorb onto the metal precursor surface and react with Co and Ni sites. These adsorbed species induce nucleation of metal phosphides and drive the outward diffusion of metal atoms and inward diffusion of phosphorus. This bidirectional diffusion promotes the gradual conversion of the precursor into crystalline CoP and Ni_2P phases, ultimately forming the final Mn-doped CoP@Ni_2P nanoneedle catalyst with microspherical structures. Possible reaction equations are as follows:

$$2NaH_2PO_2 \cdot H_2O \triangleq Na_2HPO_4 + H_2O + PH_3\uparrow$$

$$4Co^{2+} + 2PH_3 \triangleq 4CoP + 6H^+ + H_2\uparrow$$

$$8Ni^{2+} + 2PH_3 \triangleq 4Ni_2P + 6H^+ + H_2\uparrow$$

CoP@Ni_2P and Mn-CoP@Ni_2P form through a one-step hydrothermal reaction followed by annealing, and Figure 2 shows their phosphorized microstructures. As shown in Figure 2a, the undoped CoP@Ni_2P sample exhibits slender nanoneedles with lengths of approximately 200–300 nm, which are tightly intertwined and uniformly anchored on the three-dimensional nickel foam substrate. In contrast, the Mn-doped Mn-CoP@Ni_2P (Figure 2b) displays a more robust overall structure, with nanoneedles arranged in a more dispersed manner, thereby providing a larger accessible surface area that facilitates interfacial charge transfer and mass transport.

The TEM image in Figure 2c reveals that the catalyst maintains a well-defined nanoneedle morphology with diameters on the order of tens of nanometers. The nanoneedles are composed of numerous ultrafine nanoparticles that are closely interconnected, forming a rough and porous internal structure. Such a nanoparticle-assembled architecture increases the structural roughness and generates abundant surface defects, which are beneficial for exposing more catalytically active sites. In addition, the presence of numerous grain boundaries between the interconnected nanocrystallites may facilitate interfacial electron transport and shorten charge-transfer pathways during the electrocatalytic process. The porous nanoneedle framework also provides open channels for electrolyte penetration and gas diffusion, which can effectively improve mass transport and enhance the overall electrocatalytic performance. High-resolution TEM (Figure 2d) further reveals clear lattice fringes with interplanar spacings of 0.203 nm and 0.223 nm, which can be assigned to the (211) plane of CoP and the (111) plane of Ni_2P, respectively. Compared with the typical lattice spacings of pristine CoP (≈ 0.202 nm) and Ni_2P (≈ 0.221 nm), a slight lattice expansion is observed after Mn incorporation. This subtle increase in lattice spacing indicates that Mn atoms are successfully incorporated into the phosphide lattice, inducing local lattice distortion. Such distortion is generally attributed to the difference in ionic radius and electronic configuration between Mn and the host metal atoms, which leads to structural strain and charge redistribution within the lattice. The resulting lattice modulation can alter the local electronic environment of the active sites and promote electron transfer across the CoP@Ni_2P heterointerface. Moreover, the lattice distortion may generate additional defect sites and unsaturated coordination environments, which are favorable for optimizing the adsorption–desorption behavior of reaction intermediates during electrocatalysis. As shown from the selected area electron diffraction (SAED) pattern in Figure 2e, the sample exhibits typical polycrystalline ring diffraction characteristics. The crystal planes of CoP (111), (211), (202) and Ni_2P (111), (201), (210) can sequentially indexed based on the radius and intensity of diffraction rings. The simultaneous appearance of multiple diffraction rings

indicates that CoP and Ni_2P coexist in the sample and form a polycrystalline structure without generating additional impurities.

The crystal structures of CoP@Ni_2P is analyzed by XRD analysis. As shown in Figure 2(f), the three strong diffraction peaks at 44.5°, 51.8°, and 76.2° correspond to the (111) and (200) planes of NF (JCPDS No. 65-2865) [26]. The diffraction peaks observed at 31.6°, 36.3°, 46.2°, 48.1° and 56.0° for CoP@Ni_2P are assigned to the (011), (111), (112), (211) and (202) planes of CoP (JCPDS No. 65-1474). Simultaneously, the peaks at 40.7°, 44.6°, 47.6°, 51.5° and 54.8° match well with the (111), (201), (210), (300) and (211) planes of Ni_2P (JCPDS No. 32-0306) [26, 27]. Meanwhile, the XRD magnification image in Figure S1 shows that the XRD diffraction peaks shift to the left after Mn doping, which corresponds to the increased lattice spacing observed in HRTEM analysis due to Mn doping. The XRD patterns confirm the successful synthesis of the bimetallic phosphides and indicate that Mn doping into CoP@Ni_2P does not induce new crystalline phases. The EDX elemental mappings (Figure 2g) also reveal homogeneous distributions of Co, Ni, Mn, and P, suggesting that both the phosphorization and Mn doping processes are well accomplished.

XPS analysis examines CoP@Ni_2P before and after Mn doping to elucidate how Mn regulates its surface electronic structure and valence states. As shown in Figure 3a, both CoP@Ni_2P and Mn–CoP@Ni_2P exhibit typical Ni 2p $2p_{3/2}$ and Ni $2p_{1/2}$ peaks located at approximately 857.5 eV and 875.0 eV, respectively, with their corresponding satellite peaks appearing near 862.5 eV and 880.0 eV [26]. The Co $2p_{3/2}$ and Co $2p_{1/2}$ peaks are located at 782.5 eV and 798.3 eV, corresponding to Co^{2+} species, and their satellite peaks are also clearly identifiable [27]. Notably, after Mn doping, the 2p3/2 peak associated with Ni–Ox coordination shows a negative shift of about 0.78 eV; similarly, the 2p3/2 peak representing Co–Ox in the Co 2p spectrum also shows a low-BE shift of about 0.24 eV. This phenomenon can be attributed to the difference in electronegativity among the constituent elements. Mn (1.55) possesses a lower electronegativity than Ni (1.91) and Co (1.88), facilitating electron transfer from Mn to the adjacent Ni and Co atoms. Consequently, the increased electron density around Ni/Co weakens the core–level electron binding, leading to the observed negative shift in binding energy. Meanwhile, the incorporation of Mn reconstructs the local coordination environment of Ni and Co, increasing their electron cloud density and strengthening the d-electron back-donation effect. According to the d-band theory, modulation of the electronic structure can shift the d-band center of transition metal catalysts, thereby tuning the adsorption strength of reaction intermediates and optimizing catalytic performance [28]. Downshifting the d-band center induced by Mn doping weakens the binding strength of intermediates, thus optimizing the adsorption–desorption equilibrium of H* for HER and OH*, O* and OOH* for OER. This electronic modulation facilitates electron transfer at the metal centers and the adsorption of oxygen-containing intermediates during the OER process [29]. In addition, typical M–P (metal–phosphorus) bonding peaks can be observed in the low-BE region for both Ni and Co, indicating that metals and phosphorus form stable covalent/ionic hybrid bonds and exhibit significant charge-transfer behavior, confirming the integrity of the metal phosphide framework. In the P 2p spectrum shown in Figure 3c, the peak near 134.5 eV is attributed to the inevitably formed surface P–O bond; its slight

shift of about 0.2 eV after Mn doping further indicates that the local electronic environment is affected by the Mn substitution effect. As presented in Figure 3d, the high-resolution Mn 2p XPS spectrum, upon deconvolution, clearly resolves the coexistence of multiple mixed valence states of Mn, including Mn^{2+}, Mn^{3+} and Mn^{4+}. Among them, the detected Mn^{4+} signal is tentatively attributed to the partial oxidation of surface Mn species upon exposure to ambient air, which is consistent with previously reported observations[30].

3.2 Electrocatalytic HER performance

The electrocatalytic HER activity of the Mn-CoP@Ni_2P catalyst was evaluated in a conventional three-electrode system in 1.0 M KOH electrolyte. LSV curves presented in Figure 4a show that Mn-CoP@Ni_2P exhibits the most outstanding HER activity with an overpotentials at a current density of 61.7 mV at 10 mA cm^{-2}. As shown in Figure 4b, The Mn-CoP@Ni_2P shows a Tafel slope of 40 mV dec^{-1}, which is much lower than that of CoP (67 mV dec^{-1}) and CoP@Ni_2P (49.9 mV dec^{-1}), indicating its faster reaction kinetics. To obtain more reliable kinetic parameters, steady-state currents derived from chronoamperometric measurements at different applied potentials were used to reconstruct the polarization curves and corresponding Tafel plots, thereby minimizing the influence of capacitive currents during conventional LSV measurements (Figure S4). As shown in Figure S4a, the two curves are consistent within a certain error range. Additionally, the ECSA value of the electrocatalyst is a key factor influencing the efficient electrochemical performance [31,32]. The ECSA of the catalysts calculated based on the the double layer capacitance (C_{dl}) using CV curves. As expected, the Mn-CoP@Ni_2P catalyst exhibited the largest C_{dl} value of 164.4 mF cm^{-2} (Figure 4c), which is significantly higher than that of CoP (12.1 mF cm^{-2}) and CoP@Ni_2P (58.3 mF cm^{-2}). This result indicates that the synergistic effect between Mn doping and the CoP@Ni_2P heterointerface endows the catalyst with a larger ECSA and more exposed active sites. The results are consistent with the SEM morphology analysis.

To further evaluate the intrinsic catalytic activity, the turnover frequency (TOF) was calculated based on the number of active sites estimated from the ECSA (Figure S2). At an overpotential of 100 mV, the TOF of Mn-CoP@Ni_2P reaches 0.42 s^{-1}, which is approximately 2.5 times higher than that of CoP@Ni_2P (0.17 s^{-1}) and 8 times higher than that of CoP (0.05 s^{-1}), confirming the superior intrinsic HER activity of Mn-CoP@Ni_2P. The mass activity of Mn-CoP@Ni_2P at an overpotential of 100 mV reaches 125 A g^{-1}, which is 3.2 times higher than CoP@Ni_2P (39 A g^{-1}) and 12.5 times higher than CoP (10 A g^{-1}), further demonstrating the excellent catalytic efficiency per unit mass. The enhanced intrinsic activity can be attributed to the interfacial coupling between CoP and Ni_2P together with the electronic modulation induced by Mn incorporation. The formation of the CoP@Ni_2P heterointerface generates a built-in electronic interaction that promotes charge redistribution across the interface, facilitating more efficient electron transfer during the HER process. Meanwhile, Mn incorporation can tune the local electronic structure of the phosphide lattice and introduce electron-rich active centers, which improves the adsorption–desorption balance of hydrogen intermediates. Such electronic coupling across the

heterointerface effectively lowers the charge-transfer resistance and accelerates the proton–electron coupling step, thereby enhancing the intrinsic turnover rate of active sites. In addition, the heterostructured interface may provide additional catalytically active boundaries that facilitate interfacial electron transport and intermediate migration, collectively contributing to the markedly improved TOF and mass activity observed for Mn-CoP@Ni_2P [31,32].

EIS measurements reveal that Mn-CoP@Ni_2P exhibits the smallest semicircle in the high-frequency region, indicating the smallest charge-transfer resistance and the fastest reaction kinetics during the four-electron transfer process. Due to the enhanced conductivity and improved electron transport arising from the interfacial coupling between CoP and Ni_2P. The obtained impedance data were fitted using an equivalent circuit model of Rs (RctCPE), where Rs represents the solution resistance, Rct denotes the charge-transfer resistance, and CPE corresponds to the constant phase element describing the non-ideal capacitive behavior at the electrode–electrolyte interface. Meanwhile, the charge transfer resistance (Rct) of Mn-CoP@Ni_2P is 0.48 Ω, which is lower than that of CoP (3.94 Ω) and CoP@Ni_2P (0.59 Ω) (Figure 4d). The fitting procedure was carried out using ZView software, and the fitted curves were presented as smooth lines overlaid on the experimental Nyquist plots (Figure 4d). The fitted curves show a high degree of coincidence with the original experimental Nyquist curves, confirming the excellent fitting quality and the reliability of the extracted impedance parameters.

To gain deeper insight into the electrochemical processes, distribution of relaxation times (DRT) analysis was performed on the EIS data, which represents a novel approach for mechanistic understanding of Mn-doped phosphide electrocatalysts that goes beyond conventional EIS fitting and DFT calculations [24]. The DRT spectra (Figure 4e) reveal that the DRT peaks can be assigned to different electrochemical processes based on their characteristic relaxation times: (i) high-frequency features ($\tau < 10^{-3}$ s) correspond to double-layer charging and solution resistance; (ii) mid-frequency peaks ($\tau \sim 0.01$-0.1 s) are attributed to charge transfer at the heterointerface between CoP and Ni_2P phases; (iii) low-frequency peaks ($\tau \sim 1^{-10}$ s) reflect diffusion-controlled processes and adsorption/desorption of reaction intermediates (H*). The DRT spectra partition the polarization resistance into three distinct regimes, where the peak intensity directly reflects the magnitude of the resistive loss associated with each step. Significantly, the low-frequency regime ($\tau \approx 10$ s) exhibits the highest peak amplitude across all samples, identifying the adsorption/desorption of H intermediates and associated mass transport as the dominant, rate-limiting processes governing the HER kinetics. Notably, the introduction of Mn doping leads to a shift of the dominant DRT pmeak toward higher frequencies (shorter relaxation times), indicating accelerated charge transfer kinetics. This observation is consistent with the XPS analysis showing enhanced electron density at Co and Ni sites after Mn incorporation, which facilitates electron transfer during the HER process.

Additionally, the Bode plots for the HER process reveal distinct impedance response characteristics among the three catalysts across the entire investigated frequency range. As shown in the |Z|-f plots (Figure 4f), the impedance modulus of all samples decreases gradually with increasing frequency, which

reflects the transition of the rate-determining step of the HER electrocatalytic process: the low-frequency region is dominated by mass transport and the adsorption-desorption process of reaction intermediates, the mid-frequency region is controlled by the interfacial charge-transfer kinetics of the Faradaic reaction, and the high-frequency region is governed by the ohmic resistance of the electrochemical system. Notably, both CoP@Ni_2P and Mn-CoP@Ni_2P exhibit significantly lower |Z| values than pristine CoP throughout the entire frequency range, suggesting that the incorporation of Ni_2P effectively reduces the interfacial charge-transfer resistance and facilitates electron transport. In particular, Mn-CoP@Ni_2P displays the lowest impedance in the low- and medium-frequency regions, implying more favorable interfacial kinetics. The phase angle–frequency plots (Figure 4g) further provide insight into the relaxation behavior of the electrode/electrolyte interface. All samples exhibit a characteristic phase angle maximum in the intermediate frequency region, which is typically associated with the charge-transfer process at the interface. Compared with CoP and CoP@Ni_2P, the phase peak of Mn-CoP@Ni_2P shifts toward higher frequencies, indicating a smaller characteristic relaxation time constant ($\tau_o=1/2\pi f_0$) and thus a faster interfacial charge-transfer process [32]. These results suggest that the synergistic effect of Mn incorporation and the formation of the Ni_2P-based heterostructure effectively optimizes the electronic structure and accelerates the HER kinetics.

The HER stability of Mn-CoP@Ni_2P is measured by CV and chronopotentiometry, as shown in Figure 4h [33]. The chronopotentiometry curve of Mn-CoP@Ni_2P shows that the current density changes very little within 20 h, and the LSV curve of Mn-CoP@Ni_2P obtained before and after scanning of 20 h cycles also do not change significantly (inset Figure 4h), indicating the high durability of Mn-CoP@Ni_2P. The outstanding catalytic stability and activity can be attributed to the synergistic effect of Mn doping and the CoP@Ni_2P heterointerface. Specifically, Mn incorporation effectively modulates the electronic structure of the catalyst, while the strong interfacial coupling between CoP and Ni_2P facilitates efficient charge redistribution and electron transfer. These combined effects stabilize the catalytic surface and maintain the intrinsic activity of active sites, thereby enabling durable and efficient HER performance [34]. Compared with recently reported electrocatalysts, Mn-CoP@Ni_2P demonstrates superior HER performance (Figure 4i) [46-53], specific performance data are shown in Table S1.

3.3 Electrocatalytic OER performance

The OER activity of the Mn-CoP@Ni_2P electrocatalyst is examined under the same conditions as HER. As depicted in Figure 5a, Mn-CoP@Ni_2P exhibits the most outstanding and remarkably high OER activity with an overpotentials at a current density of 122 mV at 10 mA cm^{-2}. In addition, the Tafel slope of Mn-CoP@Ni_2P is only 64.09 mV·dec^{-1} (Figure 5b), significantly lower than that of CoP (70.5 mV·dec^{-1}) and CoP@Ni_2P (68.4 mV·dec^{-1}), demonstrating higher reaction kinetics efficiency of Mn-CoP@Ni_2P. To eliminate the influence of capacitive currents during potential scanning, steady-state currents obtained from chronoamperometry at different potentials were used to reconstruct the polarization curves and corresponding Tafel plots (Figure S5). The C_{dl} values extracted from the CV

measurements are shown in Figure 5c. The Mn-CoP@Ni_2P shows a C_{dl} value of 74.9 mF cm^{-2}, compared to CoP (11.4 mF cm^{-2}) and CoP@Ni_2P (72.2 mF cm^{-2}). It is noted that the C_{dl} values measured under OER conditions differ from those under HER conditions, which can be attributed to the partial surface reconstruction and oxidation of the phosphide surface during OER operation. Meanwhile, the Nyquist plots in Figure 5d illustrate that the Rct of Mn-CoP@Ni_2P (0.69 Ω) is much smaller than that of CoP (1.22 Ω) and CoP@Ni_2P (1.13 Ω), indicating that Mn-CoP@Ni_2P has excellent electron transfer performance during the OER process [35]. EIS measurements show a clear distinction in charge-transfer behavior among the three samples. Mn-CoP@Ni_2P sample presents the smallest semicircle in the high-frequency region, reflecting its low interfacial resistance and rapid electron-transfer kinetics during the OER process. When Ni_2P is introduced, the semicircle radius decreases noticeably, which suggests that the electronic interaction between CoP and Ni_2P improves the overall conductivity and accelerates charge migration across the heterointerface. The reduced electrochemical impedance after Mn doping can be attributed to the modulation of the electronic structure and interfacial charge-transfer processes, where Mn incorporation promotes charge carrier transport through defect-mediated electronic redistribution while simultaneously lowering the interfacial charge-transfer barrier at the electrode–electrolyte interface [36]. The Figure displays the equivalent circuit and the corresponding fitted curves, which closely match the experimental data. This agreement confirms that the selected model accurately captures the interfacial response characteristics. Overall, the Mn-CoP@Ni_2P electrode demonstrates a clear advantage in charge transport, forming a solid electronic foundation that supports its enhanced electrocatalytic activity [37, 38].

Furthermore, the DRT analysis (Figure 4e) of OER EIS data further confirms the superior kinetics of Mn-CoP@Ni_2P. The Bode plots similarly exhibit a pronounced frequency-dependent impedance behavior. As shown in the |Z|–f curves (Figure 5f), the impedance modulus of all catalysts decreases continuously with increasing frequency. However, CoP@Ni_2P and Mn-CoP@Ni_2P show substantially lower |Z| values than pristine CoP in the low-frequency region, indicating that the heterostructure significantly decreases the charge-transfer resistance and improves electron transport during the OER process. Among the three samples, Mn-CoP@Ni_2P maintains relatively low impedance values across the medium-to-high frequency region, reflecting more efficient interfacial charge transport. The phase angle–frequency plots (Figure 5g) reveal noticeable phase transitions in the intermediate frequency region for all samples, which correspond to interfacial charge-transfer and surface reaction processes. Compared with pristine CoP, the phase peak of Mn-CoP@Ni_2P shifts toward higher frequencies and becomes relatively broader, implying a reduced relaxation time constant and more rapid interfacial reaction kinetics. This behavior suggests that Mn modulation combined with Ni_2P coupling effectively tailors the electronic structure at the electrode interface, enhances charge-transfer capability, and thereby promotes the overall OER reaction kinetics. Compared with CoP and CoP@Ni_2P, Mn-CoP@Ni_2P has the smallest overpotential, Tafel slope and Rct, proving that the synergistic effect of the heterostructure and Mn doping in Mn-CoP@Ni_2P can improve the OER performance.

More importantly, Figure 5h demonstrates the remarkable durability of Mn-CoP@Ni_2P. The chronopotentiometry curve of Mn-CoP@Ni_2P shows that the current density is almost negligible over 20 h (Figure 5h), and the LSV curve of Mn-CoP@Ni_2P obtained before and after scanning of 20 h cycles also shows almost no change (inset Figure 5h), indicating the excellent OER stability and durability of Mn-CoP@Ni_2P. In comparison to electrocatalysts reported in recent years, this system shows outstanding performance. (Figure 5i) [54-61], specific performance data are shown in Table S2.

3.4 pH-Dependent Electrocatalytic Performance

To investigate the influence of electrolyte pH on the electrocatalytic performance, polarization curves were recorded over a series of electrolytes with different pH values under both alkaline and acidic conditions (Figure S3). LSV measurements were conducted in both acidic and alkaline electrolytes to evaluate the catalytic activity of Mn-CoP@Ni_2P. For the acidic tests, 0.1 M, 0.3 M, 0.5 M, and 1.0 M H_2SO_4 were employed, corresponding to a pH range of approximately 0.7 to 0.1. For the alkaline tests, 0.1 M, 1.0 M, 3.0 M, and 5.0 M KOH were used, with a pH range of about 13.0 to 15.0.

As shown in Figures S3a and S3b, the HER and OER responses in alkaline media exhibit noticeable variations with pH. With increasing pH from 13.0 to 15.0, the polarization curves gradually shift, indicating that the catalytic current density and reaction onset potential are sensitive to the hydroxide ion concentration in the electrolyte. Under strongly alkaline conditions, the elevated OH^- concentration facilitates the formation and stabilization of adsorbed hydroxyl intermediates (OH, O, OOH*), which promotes surface redox processes and accelerates interfacial electron transfer between the catalyst surface and the electrolyte. In addition, the higher ionic strength at elevated pH can enhance charge transport within the electrical double layer, thereby reducing interfacial charge-transfer resistance and improving overall electron transport kinetics. Similarly, the catalytic behavior in acidic media (Figures S3c and S3d) also shows a clear dependence on pH value. As the pH value changes from 0.1 to 0.7, the polarization curves display systematic shifts in both current density and overpotential, reflecting the influence of proton concentration on the reaction kinetics. In acidic environments, the HER process is predominantly governed by proton-coupled electron transfer, where the availability of solvated H^+ directly affects the Volmer step ($H^+ + e^- \rightarrow H^*$) [39-42]. At lower pH values, the higher proton activity facilitates faster electron–proton coupling at the catalyst surface, enabling more efficient formation and subsequent recombination or desorption of hydrogen intermediates. Conversely, a slight decrease in proton concentration can increase the kinetic barrier for proton reduction, leading to observable shifts in the polarization behavior. These observations demonstrate that the electrocatalytic activity of Mn-CoP@Ni_2P is closely related to the electrolyte pH, where variations in proton or hydroxide ion concentration affect the adsorption and conversion of reaction intermediates during the electrochemical process. From a mechanistic perspective, the electrolyte pH modulates both the proton/hydroxide availability and the interfacial electron-transfer pathway, thereby influencing the kinetics of proton-

coupled or hydroxide-mediated electron transfer steps. The results highlight that electrolyte pH plays a critical role in regulating the catalytic response of the electrode across a broad pH range [43,44].

3.5 Overall water splitting performance

To evaluate the overall water splitting performance, a dual electrode alkaline electrolysis cell (Figure 6a) was assembled using two identical Mn-CoP@Ni_2P electrodes as both the anode and cathode in 1.0 M KOH solution. As presented in Figure 6b, the LSV polarization curve of Mn-CoP@Ni_2P requires the lower cell voltages of 1.48 and 1.73 V at current densities of 10 and 100 mA·cm^{-2}. Meanwhile, Chronoamperometric stability test of the Mn-CoP@Ni_2P||Mn-CoP@Ni_2P electrode system over 24 h. The current density remaining nearly constant with only slight fluctuations throughout the testing period, indicating the excellent long-term electrochemical stability of the electrode (Figure 6c). In summary, the synthesized Mn-CoP@Ni_2P electrode exhibits excellent activity as a bifunctional catalyst for practical applications in the field of water splitting [45].

4 Conclusions

In summary, Mn-doped CoP@Ni_2P nanoneedle arrays were successfully in situ fabricated on nickel foam via a facile two-step hydrothermal growth and phosphorization strategy. The hierarchical nanoneedle array structure provides abundant exposed active sites and efficient pathways for electron transfer and mass transport. Owing to the synergistic effects of Mn doping and the CoP@Ni_2P heterointerface, the optimized Mn-CoP@Ni_2P electrode exhibited excellent bifunctional electrocatalytic performance, delivering low overpotentials of 61.7 mV for the HER and 122.0 mV for the OER at 10 mA cm^{-2} in alkaline electrolyte, and only requiring a cell voltage of 1.48 V to drive overall water splitting at 10 mA cm^{-2}. Mechanistic analyses indicate that Mn incorporation modulates the electronic structure and promotes charge redistribution at the heterointerface, thereby optimizing intermediate adsorption and accelerating reaction kinetics. These results highlight an effective strategy for designing high-performance non-noble metal electrocatalysts for water splitting.

Declarations

Author Contributions

Yu Dong conducted experimental synthesis, characterization, and electrochemical testing. Xuan Zhao, Zhijie Wang and Ende Wang provided significant assistance in data analysis and manuscript writing. Yusheng Qiu contributed to the preparation and characterization of the materials. Yongli Tong and Naikun Sun supervised the research, designed the experiments, and revised the manuscript. All authors have reviewed and approved the final manuscript.

Data Availability Statement

The data that support the findings of this study are available from the corresponding.

Conflicts of interest

There are no conflicts to declare.

Acknowledge

The work was supported by the Special Fund of Basic scientific Research Business expenses of undergraduate universities in Liaoning Province (LJ212410144004) from Liaoning Provincial Department of Education.

References

1. Franco, C. Giovannini, Recent and Future Advances in Water Electrolysis for Green Hydrogen Generation: Critical Analysis and Perspectives, *Sustainability*, 2023, **15**, 16917.
2. S. Chu, A. Majumdar, Opportunities and challenges for a sustainable energy future, *Nature*, 2012, **488**, 294–303.
3. J. Kibsgaard, I. Chorkendorff, Considerations for the scaling-up of water splitting catalysts, *Nature Energy*, 2019, **4**, 430–433.
4. M. A. Ahsan, A. R. Puente Santiago, Y. Hong, N. Zhang, M. Cano, E. Rodriguez-Castellon, L. Echegoyen, S. T. Sreenivasan, J. C. Noveron, Manganese-Doped Bimetallic $(Co,Ni)_2P$ Integrated CoP in N,S Co-Doped Carbon: Unveiling a Compatible Hybrid Electrocatalyst for Overall Water Splitting, *Small*, 2024, **20**, 2307241.
5. C. Y. Zhang, J. X. Luo, S. J. Sun, K. L. Yuan, M. X. Ran, C. H. Li, X. M. Yan, Ultrathin NiFe layered double hydroxide nanosheets coupled with conductive carbon for highly efficient overall water splitting, *Journal of Power Sources*, 2025, **635**, 235976.
6. G. Ma, J. Ye, M. Qin, T. Sun, W. Winie, Z. Fan, L. Huang, X. Xin, Mn-doped NiCoP nanopin arrays as high-performance bifunctional electrocatalysts for sustainable hydrogen production via overall water splitting, *Nano Energy*, 2023, **115**, 108679.
7. X. Zhang, Y. Liu, Paper-based porous graphene/single-walled carbon nanotubes supported Pt nanoparticles as freestanding catalyst for electro-oxidation of methanol, *Applied Catalysis B: Environmental*, 2019, **256**, 117886.
8. S. Li, E. Li, X. An, X. Hao, Z. Jiang, G. Guan, Transition metal-based catalysts for electrochemical water splitting at high current densities: challenges and opportunities, *Nanoscale*, 2021, **13**, 12788–12817.
9. M. N. Lakhan, A. Hanan, A. Hussain, I. A. Soomro, Y. Wang, M. Ahmed, U. Aftab, H. Sun and H. Arandiyan, Transition metal-based electrocatalysts for alkaline overall water splitting: advancements, challenges, and perspectives, *Chemical Communications*, 2024, **60**, 5104–5135.

10. J. Ying, H. Wang, Strategies for Developing Transition Metal Phosphides in Electrochemical Water Splitting, *Frontiers in Chemistry*, 2021, **9**, 700020.
11. L.-M. Cao, J. Zhang, L.-W. Ding, Z.-Y. Du, C.-T. He, Metal-organic frameworks derived transition metal phosphides for overall water splitting, *Journal of Energy Chemistry*, 2022, **68**, 494–520.
12. Y. Chen, Y. Wang, H. Yang, C. Gao, H. Ding, Y. Zhao, Ultrathin two-dimensional metal–organic framework nanosheets for high-performance electrocatalysis, *Materials Chemistry Frontiers*, 2023, **7**, 6489–6505.
13. S. Che, Y. Jia, Y. Li, Design and Synthesis of Self-Supported Water-Splitting Transition Metal-Based Electrocatalysts via Electrospinning, *Catalysts*, 2025, **15**, 205.
14. Y.Liu, X. Zhang, J. Li, H. Lin, Porous Mn-doped cobalt phosphide nanosheets as highly active electrocatalysts for oxygen evolution reaction, *Chemical Engineering Journal*, 2021, **425**, 131642.
15. T. Yu, S. Kim, H. Kang, Recent Tendency on Transition-Metal Phosphide Electrocatalysts for the Hydrogen Evolution Reaction in Alkaline Media, *Nanomaterials*, 2023, **13**, 2613.
16. Y. Zhang, M. Zhang, H. Zhang, D. Han, J. Wang, R. Yang, C. Zuo, X. Chen, Bimetallic Mn and Cr co-doped nickel cobalt phosphide nanoneedle arrays as bifunctional electrocatalysts for overall water splitting, *Fuel*, 2025, **396**, 135348.
17. H. Xu, X. She, H. Li, C. Wang, S. Chen, L. Diao, P. Lu, L. Li, L. Tan, J. Sun, Y. Zou, Recent Advances in Transition Metal Phosphide Electrocatalysts for Water Splitting, *Molecules*, 2024, **29**, 657.
18. Y. Gao, Y. Qiao, X. Li, C. Huang, J. Zhang, Y. Wang, X. Zou, Z. Xia, X. Yang, X. Lu, Y. Zhao, Bimetallic site substitution of NiCoP nanoneedles as bifunctional electrocatalyst for boosted water splitting, *Nano Research*, 2024, **17**, 9540–9549.
19. Y.-T. Li, J. Yi, R. Qin, C. Xie, L. Zhao, X. Lang, Q. Jiang, Dual-site engineered NiCoP nanosheets for highly efficient overall water splitting, *Journal of Colloid and Interface Science*, 2024, **661**, 690-699.
20. K. Tao, D. Zhang, R. Qin, X. Li, C. Xie, L. Zhao, X. Lang, Q. Jiang, Electronic structure modulation of NiCoP nanosheets for highly efficient electrocatalytic water splitting, *Dalton Transactions*, 2024, **53**, 1757-1765.
21. K. Chen, Y.-H. Cao, G.-C. Kim, C. Kim, S. Yadav, V. Dao, I.-H. Lee, Hierarchically structured NiCoP nanosheets anchored on carbon cloth as efficient bifunctional electrocatalysts for overall water splitting, *Advanced Composites and Hybrid Materials*, 2024, **7**, 71.
22. Q. Ma, H. Jin, F. Xia, H. Xu, J. Zhu, R. Qin, H. Bai, B. Shuai, W. Huang, D. Chen, Z. Li, J. Wu, J. Yu, S. Mu, Three-dimensional hierarchical NiCoP nanosheet arrays as highly efficient bifunctional electrocatalysts for overall water splitting, *Journal of Materials Chemistry A*, 2021, **9**, 27055–27066.
23. H. Zhang, W. Liu, Z. Li, L. Qiao, K. Chi, X. Guo, D. Cao, D. Cheng, Interfacial electronic structure engineering of transition-metal phosphide nanosheets for highly efficient overall water splitting, *Advanced Science*, 2024, **11**, 2401398.
24. N. Chen, S. Che, Y.-H. Zhang, H.-Q. Li, Y.-F. Li, X.-J. He, Size effect of carbon nanotubes confined CoP–Ni_2P heterostructure via phosphorylation-induction strategy for efficient overall water splitting, *Rare Metals*, 2025, **44**, 4740–4755.

25. Y.-T. Luo, Z.-Y. Zhang, M. Chhowalla, B. Liu, Recent Advances in Design of Electrocatalysts for High-Current-Density Water Splitting, *Advanced Materials*, 2022, **34**, 2108133.
26. Y. Sun, K. Xu, C.-C. Li, Y. Li, Recent progress in cobalt-based phosphide electrocatalysts for overall water splitting, *Journal of Materials Chemistry A*, 2020, **8**, 13415–13436.
27. T. Liu, X. Ma, D. Liu, S. Hao, G. Du, Y. Ma, A. M.Asiri, X. Sun and L. Chen, Self-Supported CoP Nanosheet Array: A Highly Efficient 3D Hydrogen-Evolving Cathode for Electrochemical Water Splitting, *ACS Catalysis*, 2017, **7**, 98–102.
28. F. Huang, J. Wang, M. Wang, C. Zhang, Y. Xue, J. Liu, T. Xu, N. Cai, W. Chen and F. Yu, Hierarchical NiCoP nanosheet arrays as highly efficient bifunctional electrocatalysts for overall water splitting, *Colloids and Surfaces A*, 2021, **623**, 126526.
29. H. Zhang, W. Liu, Z. Li, L. Qiao, K. Chi, X. Guo, D. Cao and D. Cheng, Self-Reconstruction of Transition-Metal Phosphides into Active Oxyhydroxides for Highly Efficient Overall Water Splitting, *Advanced Science*, 2024, **11**, 2307890.
30. X. Liu, Y. Qiao, X. Li, C. Huang, J. Zhang, Y. Wang, X. Zou, Z. Xia, X. Yang, X. Lu, Y. Zhao, Unveiling the role of lattice-oxygen participation in metal phosphide electrocatalysts for efficient alkaline water splitting, *Nature Communications*, 2021, **12**, 1785.
31. N. Laschuk, E. Bradley, O. Zenkina, Recent advances in transition metal phosphide electrocatalysts for water splitting, *RSC Advances*, 2021, **11**, 27925.
32. Y. Zhang, Y.-T. Li, J. Yi, R. Qin, C. Xie, L. Zhao, X. Lang, Q. Jiang, Boosting alkaline hydrogen evolution reaction on Ni–Co–P nanosheets by regulating the electronic structure of active sites, *Advanced Energy Materials*, 2020, **10**, 1903101.
33. L. Zhang, Y.-T. Li, J. Yi, R. Qin, C. Xie, L. Zhao, X. Lang, Q. Jiang, Electronic structure modulation of NiCoP nanosheets for highly efficient electrocatalytic hydrogen evolution in alkaline media, *Journal of Materials Chemistry* A, 2022, **10**, 845-853.
34. F. Yu, H. Zhou, Y. Zhang, G. Li, Y. Xiong, High-performance bifunctional porous non-noble metal phosphide catalyst for overall water splitting, *Nature Communications* , 2018, **9**, 2551.
35. Y. Sun, J. Dai, H. Lv, L. Dong, Z. Wang, H. Feng, B. Meng and Z. Li, Interface-engineered transition-metal phosphide heterostructures for highly efficient overall water splitting, *Advanced Functional Materials*, 2025, **35**, 2401234.
36. X. Yu, J. Zhao, M. Johnsson, Interfacial Engineering of Nickel Hydroxide on Cobalt Phosphide for Alkaline Water Electrocatalysis, *Advanced Functional Materials*, 2021, **31**, 2101578.
37. M. Zhang, H. Xu, H. Yang, X. Shang, M. Yuan, Y. Fu, Y. Xiao, S. Wang, X. Wang, B. Jia, S. Li, T. Ma, Electronic Modulation of Nickel Cobalt Phosphide Nanosheets by Ce Doping for Efficient Overall Water Splitting, *Small*, 2025, **21**, 2504837.
38. T. Zhao, B. Gong, G. Xu, J. Jiang, L. Zhang, In situ surface reconstruction of heterostructure $Ni_2P/CoP/FeP_4$ nanowires network catalyst for high-current-density overall water splitting, *Chinese Journal of Catalysis*, 2024, **61**, 269–280.

39. C. Devi, R. Yadav, S. Rana, G. C. S, Transition metal phosphides as cardinal electrocatalytic materials for alkaline hydrogen production, *Cell Reports Physical Science*, 2023, **4**, 101747.
40. H. Yin, F. Rong, Y. Xie, A review of typical transition metal phosphide electrocatalysts for hydrogen evolution reaction , *International Journal of Hydrogen Energy*, 2024, **52**, 350-375.
41. S. Liu, Z. Zhang, K. Dastafkan, Y. Shen, C. Zhao and M. Wang, Atomic-Level Modulation of Cobalt Phosphide Catalysts for Highly Efficient Overall Water Splitting, *Nature Communications*, 2023, **14**, 3275.
42. Y. Luo, P. Wang, G. Zhang, S. Wu, Z. Chen, H. Ranganathan, S. Sun, Mn-doped nickel–iron phosphide heterointerface nanoflowers for efficient alkaline freshwater/seawater splitting at high current densities, *Chemical Engineering Journal*, 2023, **454**, 140061.
43. Z. Zhao, Y. Dong, H. Ding, X. Li, X. Chang, Manganese-facilitated dynamic active-site generation on Ni_2P with self-termination of surface reconstruction for urea oxidation at high current density, *Water Research*, 2024, **249**, 121266.
44. H. Xu, J. Bi, T. Sang, W. Wang, J. Hao, Z. Li, Mn-doped Ni_2P: nanocrystal-decorated amorphous nanosheets for efficient electrooxidation of 5-hydroxymethylfurfural, *Chemical Communications*, 2023, **59**, 8440–8443.
45. K. Moradi, M. Ashrafı, A. Salimi and M. Melander, Hierarchical MoS_2@NiFeCo-Mo (doped)-Layered Double Hydroxide Heterostructures as Efficient Alkaline Water Splitting (Photo) Electro-catalysts, *Small*, 2025, **21**, 2409097.
46. Y. Ma, C. Wu, X. Feng, H. Tan, L. Yan, Y. Liu, Z. Kang, E. Wang, Y. Li, Highly efficient hydrogen evolution from seawater by a low-cost and stable CoMoP@C electrocatalyst superior to Pt/C, *Energy & Environmental Science*, 2017, **10**, 788.
47. L. Zheng, W. Hu, X. Shu, H. Zheng, X. Fang, Organic–Inorganic Hybrid Perovskite Photodetectors with High Performance and Multipurpose Applications, *Adv. Mater. Interfaces*, 2018, **5**, 1800515.
48. P. Jiang, Q. Liu, X. Sun, High-performance photodetectors based on GaN nanowires/graphene heterojunctions, Bimetallic Metal-Organic Framework-Derived Li-Storable CoPn Nanocrystals Embedded in Carbon Nanoboxes for Efficient Lithium-Ion Storage, *Nanoscale*, 2014, **6**, 13440.
49. J. Song, C. Zhu, B. Z. Xu, S. Fu, M. H. Engelhard, R. Ye, D. Du, S. P. Beckman and Y. Lin, Bimetallic Metal–Organic Framework-Derived CoP_x @Carbon Nanoboxes for Efficient Lithium Storage, *Adv. Energy Mater*, 2017, **7**, 1601555.
50. B. Zhang, J. Shan, W. Wang, P. Tsiakaras, Y. Li, Heterostructure Engineering of NiFe-LDH@NiCoP/NF for Efficient and Stable Overall Water Splitting, *Small*. 2022, **18**, 2106012.
51. Y. Ge, S. R. Craig, P. M. Ajayan, M. Ye and J. Shen, Heterostructural NiFe-LDH/NiCoP@NF Electrocatalyst with Enhanced Energy Efficiency for Overall Water Splitting, *Advanced Energy Materials*, 2018, **18**, 1800484.
52. F. Yang, S. Yang, Q. Niu, S. Huo, Z. Song and L. Song, Direct C–H functionalization of quinoline N-oxides with ethers via a cross-dehydrogenative coupling reaction, *New J Chem*, 2020, **44**, 8183–8190.

53. M. Wang, X. Liu, X. Wu, Realizing efficient electrochemical overall water electrolysis through hierarchical CoP@NiCo-LDH nanohybrids, *Nano Energy*, 2023, **114**, 108681.
54. W. Gong, H. Zhang, L. Yang, J. Wang and H. Liang, Core@shell MOFs derived Co_2P/CoP@NPGC as a highly-active bifunctional electrocatalyst for ORR/OER, *J Ind Eng Chem*, 2022, **106**, 492–502.
55. J. Zhang, L. Hao, Z. Chen, Y. Gao, H. Wang and Y. Zhang, Facile synthesis of Co-Fe layered double hydroxide nanosheets wrapped on Ni-doped nanoporous carbon nanorods for oxygen evolution reaction, *J Colloid Interface Sci*, 2023, **650**, 816–824.
56. K. Xu, H. Cheng, L. Liu, H. Lv, X. Wu, C. Wu, Y. Xie, Defect-Rich Ultrathin Cobalt Iron Phosphide Nanosheets with Abundant Surface Iron Hydroxyl Groups for Efficient Oxygen Evolution Reaction, *Nano Lett*, 2017, **17**, 578-583.
57. B. Zhang, J. Shan, J. Yu, W. Wang, W. Li, N. Li, Y. Li, Electrospun prussian blue analogue derived NiCo@N-doped carbon nanofibers as efficient and highly stable electrocatalysts for neutral overall water splitting, *Int J Hydrogen Energ*, 2021, **46**, 8871.
58. T. Xie, B. Wang, S. Yang, Q. Xu, X. Cheng, C. Zhou, J. Hu, Ultrasmall Co-NiP embedded into lantern shaped composite achieved by coordination confinement phosphorization for overall water splitting, *J. Alloys Compd*, 2022, **921**, 166111.
59. Y. Deng, Y. Cao, Y. Xia, X. Xi, Y. Wang, W. Jiang, D. Yang, A. Dong and T. Li, Self-Templated Synthesis of CoFeP@C Cage-In-Cage Superlattices for Enhanced Electrocatalytic Water Splitting, *Adv. Energy Mater*, 2022, **12**, 2202394.
60. X. Liu, Q. He, S. Xiao, X. Li, L. Chang, Y. Xiang, K. Hu, X. Niu, R. Wu and J. Chen, Realizing Efficient Overall Water Splitting by Tuning the Cobalt Content in Self-Supported Ni_x-Co_y-P Microarrays, *ChemElectroChem*, 2021, **8**, 1307–1315.
61. X. Yin, D. Lu, J. Wang, X. Lu, 2D/2D Heterojunction of Ni-Co-P/Graphdiyne for Optimized Electrocatalytic Overall Water Splitting, *ChemCatChem*, 2019, **11**, 5407–5411.

Figures

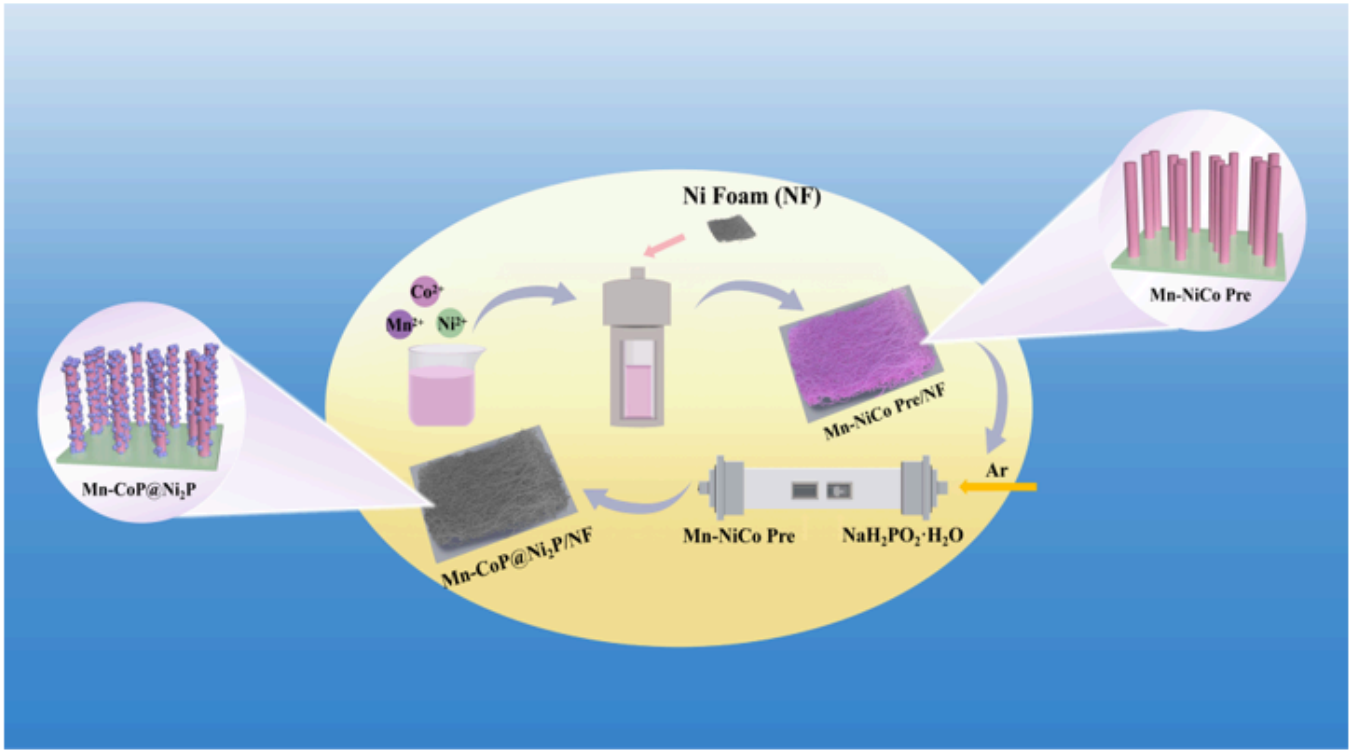


Figure 1

Schematic illustration of the synthetic procedure of Mn-CoP@Ni_2P

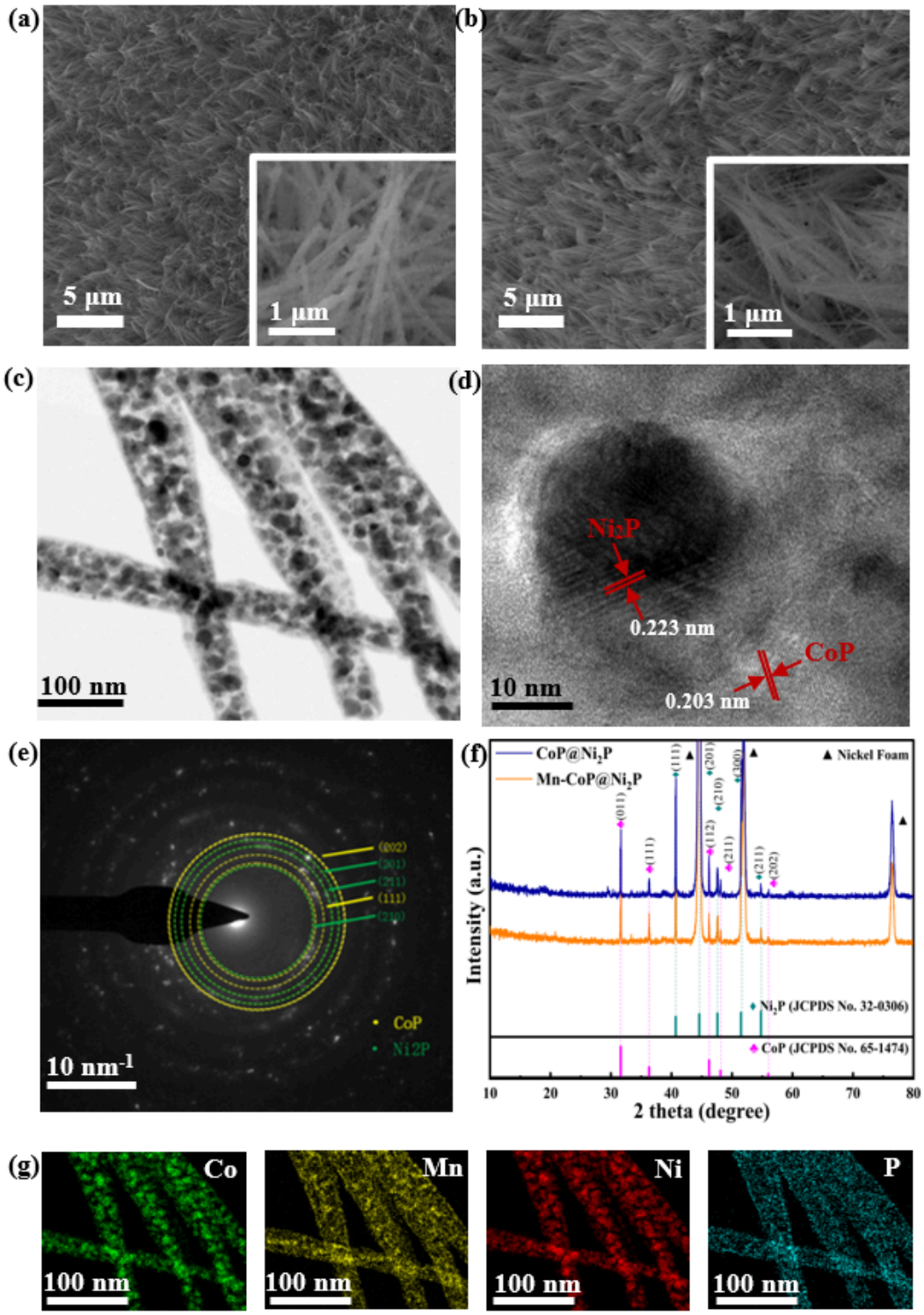


Figure 2

(a) SEM image of CoP@Ni_2P (b) SEM image of Mn-CoP@Ni_2P (c)TEM image (d) HRTEM image (e) SAED image (f) XRD patterns of CoP@Ni_2P and Mn-CoP@Ni_2P (g) EDS element mapping images of Co Mn Ni and P in Mn-CoP@Ni_2P.

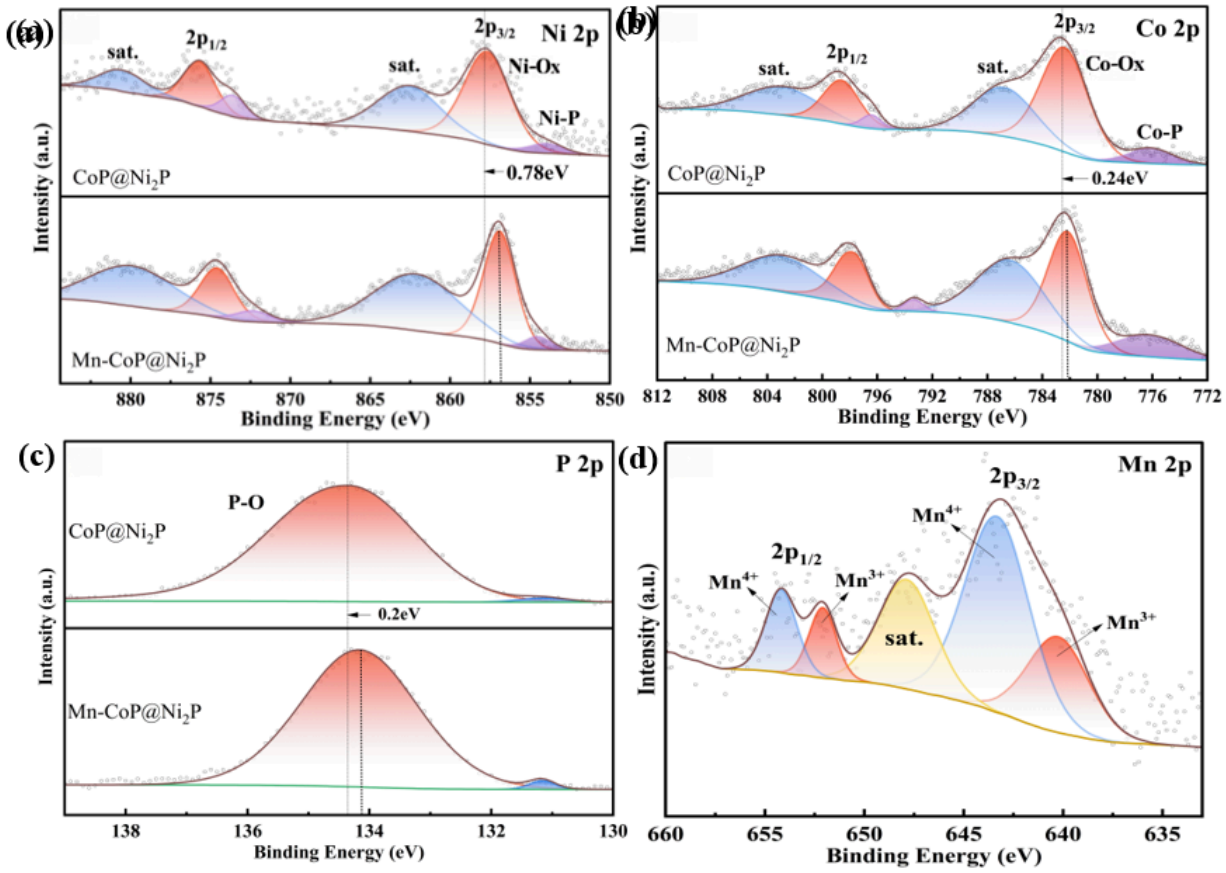


Figure 3

High-resolution XPS spectra of electrocatalysts (a) Ni 2p, (b) Co 2p, (c) P 2p and (d) Mn 2p .

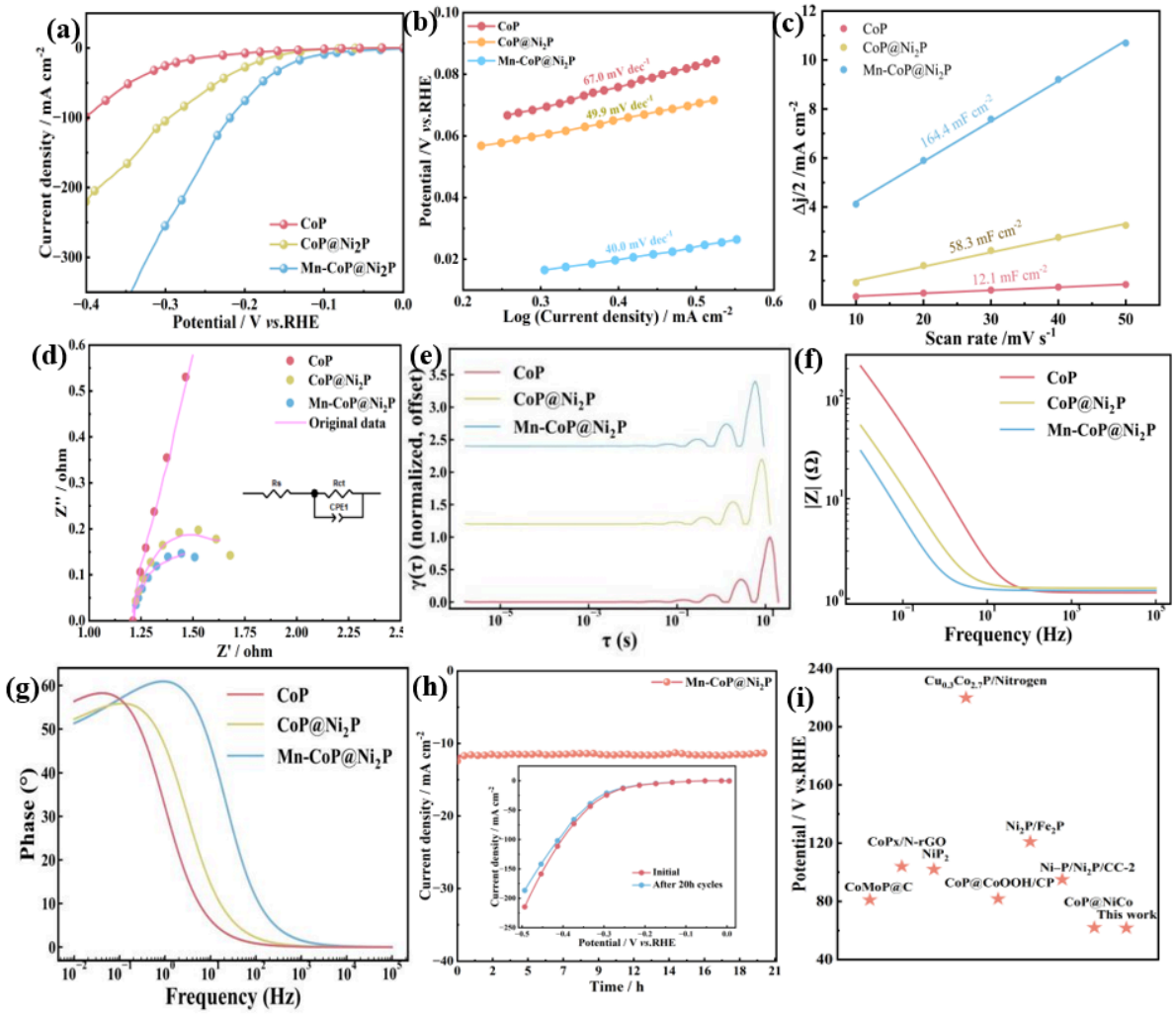


Figure 4

Electrocatalytic HER activity. (a) Polarization curves of CoP,CoP@Ni_2P,Mn-CoP@Ni_2P for HER in 1.0 M KOH solution. (b) Tafel plots. (c) C_{dl} values obtained from the linear relationship between scan rate and current density variation. (d) EIS of obtained samples. (e) DRT phase of CoP, CoP@Ni_2P, Mn-CoP@Ni_2P. (f, g)Bode phase of CoP, CoP@Ni_2P, Mn-CoP@Ni_2P. (h) Current density versus time (i–t) curves of Mn-CoP@Ni_2P Electrocatalytic HER activity and polarization curves after 20h cycles. (i) HER comparison of different overpotentials at 10 mA cm^{-2}.

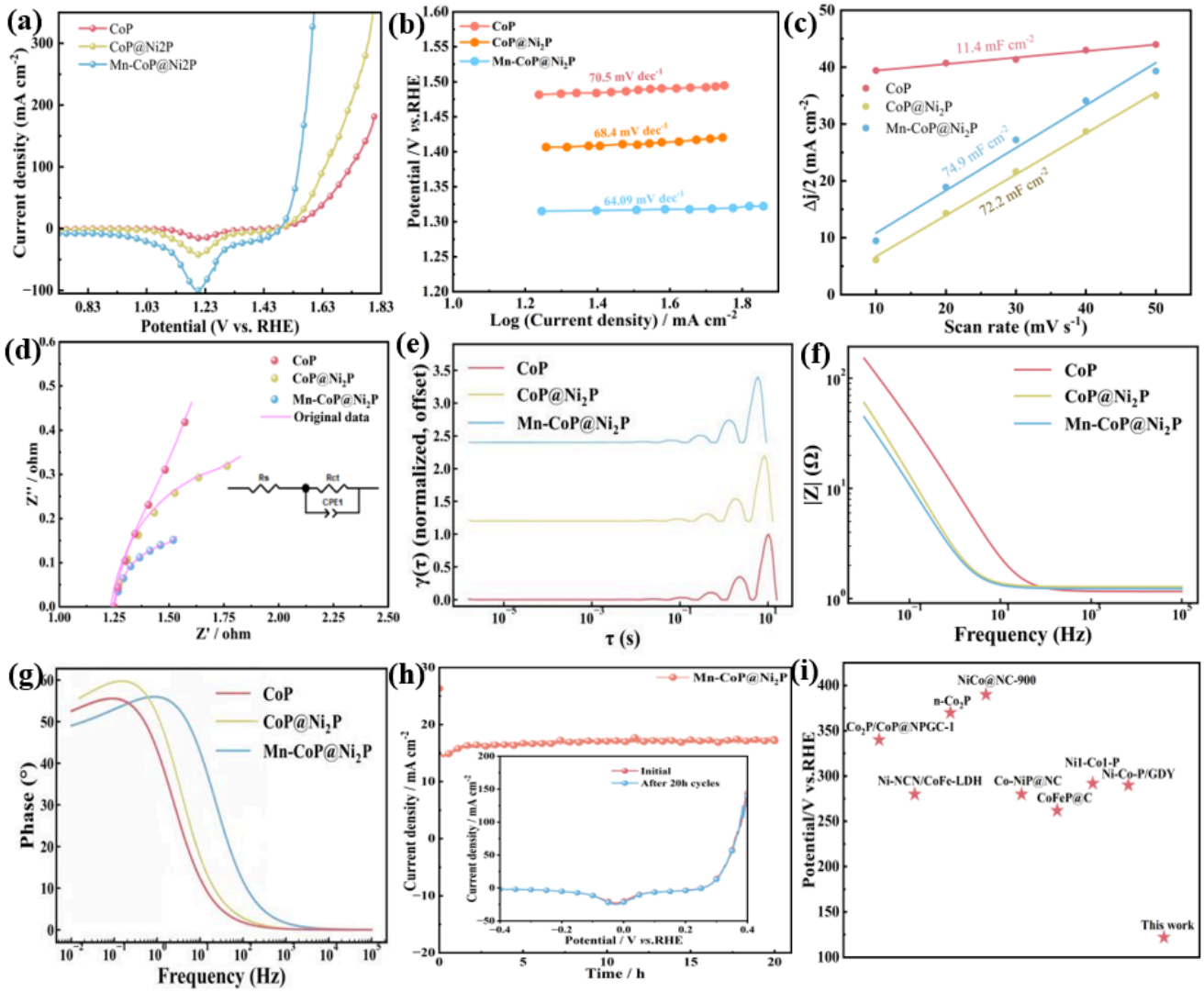


Figure 5

Electrocatalytic OER activity. (a) Polarization curves of CoP,CoP@Ni_2P,Mn-CoP@Ni_2P for HER in 1.0 M KOH solution. (b) Tafel plots. (c) C_{dl} values obtained from the linear relationship between scan rate and current density variation. (d) EIS of obtained samples. (e) DRT phase of CoP, CoP@Ni_2P, Mn-CoP@Ni_2P. (f, g)Bode phase of CoP, CoP@Ni_2P, Mn-CoP@Ni_2P. (h) Current density versus time (i–t) curves of Mn-CoP@Ni_2P Electrocatalytic OER activity and polarization curves after 20h cycles. (i) OER comparison of different overpotentials at 10 mA cm^{-2}.

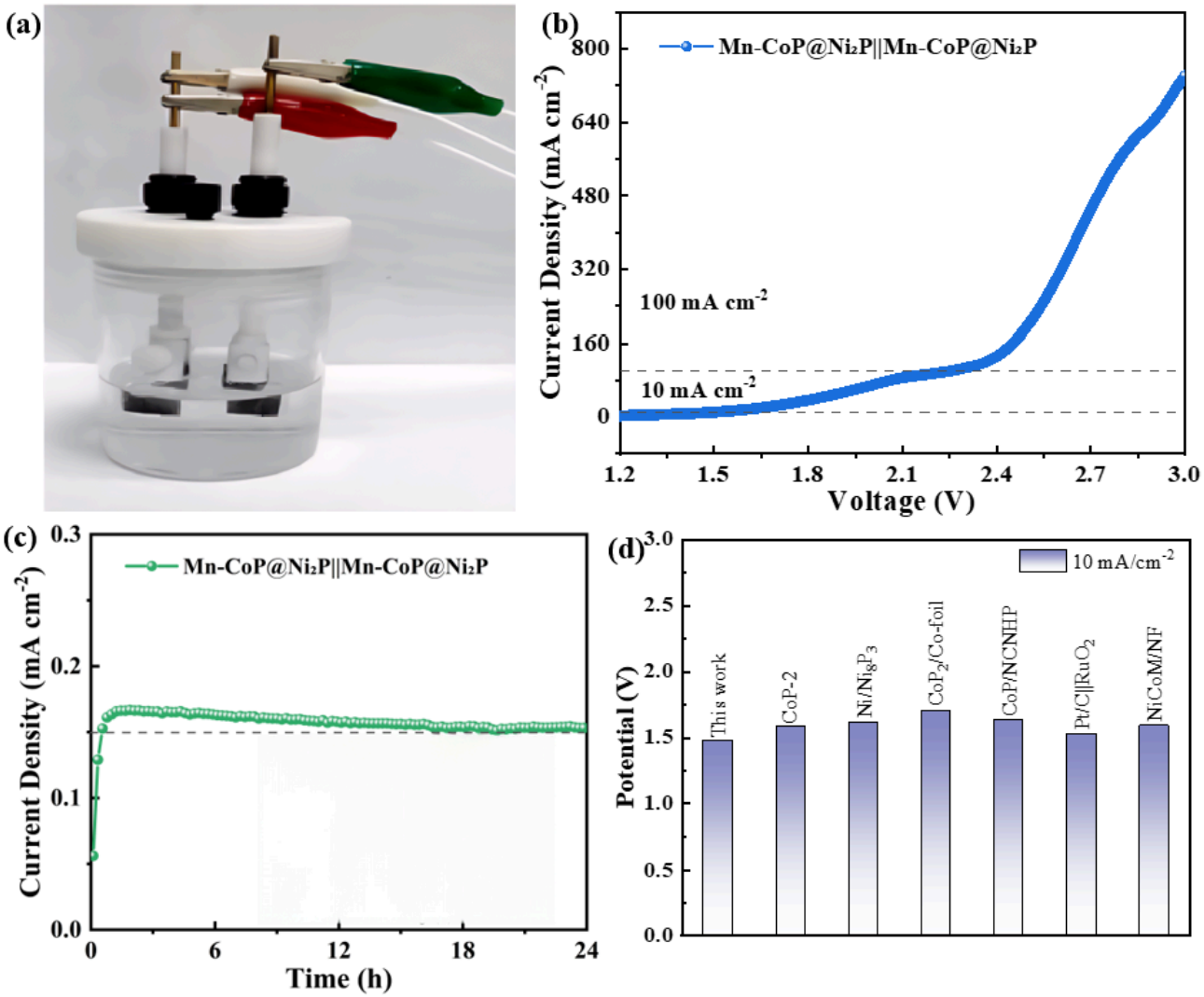


Figure 6

Overall water splitting of Mn-CoP@Ni_2P. (a) The schematic diagram of two-electrode system.(b) LSV curves of Mn-CoP@Ni_2P||Mn-CoP@Ni_2P in 1 M KOH. (c) Chronoamperometry curve of Mn-CoP@Ni_2P||Mn-CoP@Ni_2P toward overall water splitting and polarization curves of Mn-CoP@Ni_2P before and after cycles. (d)Performance comparison of water splitting between Mn-CoP@Ni_2P and reported catalysts at 10 mA·cm^{-2} respectively.

Supplementary Files

This is a list of supplementary files associated with this preprint. Click to download.

- Supportinginformation.docx